Iron-line and continuum variations in the XMM-Newton and Suzaku spectra of the neutron-star low-mass X-ray binary 4U 1636-53

Lyu, Ming; Méndez, Mariano; Sanna, Andrea; Homan, Jeroen; Belloni, Tomaso; Hiemstra, Beike

Published in:
Monthly Notices of the Royal Astronomical Society

DOI:
10.1093/mnras/stu279

Publication date:
2014

Monthly Notices
of the
ROYAL ASTRONOMICAL SOCIETY

MNRAS **440,** 1165–1178 (2014)
Advance Access publication 2014 March 19

doi:10.1093/mnras/stu279

Iron-line and continuum variations in the *XMM–Newton* and *Suzaku* spectra of the neutron-star low-mass X-ray binary 4U 1636−53

Ming Lyu,[1⋆] Mariano Méndez,[1] Andrea Sanna,[2] Jeroen Homan,[3] Tomaso Belloni[4] and Beike Hiemstra[1]

[1]*Kapteyn Astronomical Institute, University of Groningen, PO BOX 800, NL-9700 AV Groningen, the Netherlands*
[2]*Dipartimento di Fisica, Università degli Studi di Cagliari, SP Monserrato-Sestu km 0.7, I-09042 Monserrato, Italy*
[3]*MIT Kavli Institute for Astrophysics and Space Research, 70 Vassar Street, Cambridge, MA 02139, USA*
[4]*INAF - Osservatorio Astronomico di Brera, Via E. Bianchi 46, I-23807 Merate, Italy*

Accepted 2014 February 10. Received 2014 February 9; in original form 2013 November 21

ABSTRACT

We used six simultaneous *XMM–Newton* and *Rossi X-ray Timing Explorer* plus five *Suzaku* observations to study the continuum spectrum and the iron emission line in the neutron-star low-mass X-ray binary 4U 1636−53. We modelled the spectra with two thermal components (representing the accretion disc and boundary layer), a Comptonized component (representing a hot corona), and either a Gaussian or a relativistic line component to model an iron emission line at ∼6.5 keV. For the relativistic line component, we used either the DISKLINE, LAOR or KYRLINE model, the latter for three different values of the spin parameter. The fitting results for the continuum are consistent with the standard truncated disc scenario. We also find that the flux and equivalent width of the iron line first increase and then decrease as the flux of the Comptonized component increases. This could be explained either by changes in the ionization state of the accretion disc where the line is produced by reflection, or by light bending of the emission from the Comptonized component if the height at which this component is produced changes with mass accretion rate.

Key words: accretion, accretion discs – stars: neutron – X-rays: binaries – X-rays: individual: 4U 1636−53.

1 INTRODUCTION

Low-mass X-ray binaries (LMXBs) consist of a compact object (a neutron star or a black hole) and a late-type companion star with a mass of less than ∼1 $M_\odot$. Material from the outer layers of the companion is stripped off and accretes on to the compact object via the inner Lagrangian point and an accretion disc (Frank, King & Raine 2002). The inner parts of the accretion disc, and in the case of neutron stars the neutron-star surface and boundary layer, emit mostly in the X-ray band. These systems show also high-energy (up to a few 100 keV) emission, likely produced by Comptonization of the soft-X-ray photons in a hot electron corona (McConnell et al. 2000; Sanna et al. 2013). An extra hard tail has been observed in some LMXBs, e.g. GX 17+2, 4U 1636−53, GX 349+2, Sco X-1, 4U 1608−522, GX 13+1, 4U 1705−44 (Di Salvo et al. 2000b; Fiocchi et al. 2006; Paizis et al. 2006; Piraino et al. 2007).

Based on X-ray spectral and rapid variability properties, Hasinger & van der Klis (1989) classified the neutron-star LMXBs into two categories: the Z sources and the Atoll sources, owing their names to the shapes that the source traces in an X-ray colour–colour diagram. The Z sources have higher luminosities (∼0.5–1 $L_{\rm Edd}$) than the Atoll sources (0.01–0.2 $L_{\rm Edd}$; e.g. Ford et al. 2000; Done, Gierliński & Kubota 2007; Homan et al. 2007). In Atoll sources, the X-ray spectrum softens and the time-scale of the majority of the variability components decreases as the luminosity of the source generally increases (Hasinger & van der Klis 1989; van Straaten, van der Klis & Méndez 2003). More specifically, at low luminosities these sources are in the so-called hard state, in which the Comptonized component dominates the energy spectrum; this component can be reasonably described by a power law with a photon index of ∼1.6–2.5 (Yoshida et al. 1993; Méndez et al. 1997). The temperature at the inner edge of the accretion disc is relatively low, 0.3–0.5 keV (Sanna et al. 2013), and the disc usually contributes less than 20 per cent of the emission in the 1–20 keV energy range. In the truncated disc scenario (see, e.g. Done et al. 2007, and references therein), the accretion disc is truncated at a large radius in the hard state, thus being the reason for the relatively low inner-disc temperature and thermal component flux (Gierliński & Done 2003). At high luminosities, in the soft state, the disc emission in the 1–20 keV

⋆E-mail: m.lyu@astro.rug.nl

range becomes more significant. The standard accretion-disc model (Shakura & Sunyaev 1973) predicts that in this case the disc extends down to the innermost stable circular orbit (ISCO) radius, leading to a high disc temperature and a strong thermal component. Compared to the hard state, in the soft state, the inner-disc temperature increases to 0.7–1.0 keV (Sanna et al. 2013); since the number of soft photons increases as T^4, the electrons in the corona are efficiently cooled down via the inverse Compton scattering process and the Comptonized spectrum steepens (photon index ∼2–2.5; e.g. Miyamoto et al. 1993; Méndez et al. 1997). In the soft state, the thermal components dominate the X-ray spectrum below ∼20 keV, and little hard emission is detected (Gierliński & Done 2003). Both in the hard and the soft state, the neutron-star surface or boundary layer, usually fitted with a blackbody component (White, Stella & Parmar 1988; Sanna et al. 2013), contributes significantly to the emission at energies below ∼10 keV. Going from the hard to the soft state, or vice-versa, the spectra of these sources display some intermediate properties, and the source is said to be in the intermediate, or transitional, state. (These basic states receive several names depending on the class of the source; see, e.g. Hasinger & van der Klis 1989.) The mechanism driving the transition between the hard to the soft state is still unclear. However, it is generally assumed that the change of mass accretion rate and the disc geometry are connected to the state evolution (Hasinger & van der Klis 1989; Méndez et al. 1999; Lin, Remillard & Homan 2007).

Besides the emission components described above, the accretion disc is likely illuminated by the Comptonized photons and the thermal spectrum from the neutron star and its boundary layer, and as a consequence it produces a reflection spectrum (e.g. Fabian & Ross 2010). Due to the high abundance and fluorescence yield, an iron emission line at ∼6–7 keV may appear in the spectrum, with an intrinsic line width of the order of 1 eV (Basko 1978). The iron-line profile is asymmetrically broadened by the fast disc rotation (Doppler broadening) and special and general relativistic effects (e.g. Doppler boosting and gravitational redshift) near the central compact object (Fabian et al. 1989). The final line profile is determined by parameters of the system, like the inclination angle of the disc with respect to the line of sight, the inner radius of the disc, and the spin parameter of the central object. Thus, measurements of the iron-line profile provide an excellent way to study the physics and geometry of the accretion process (Bhattacharyya & Strohmayer 2007; Cackett et al. 2008; Miller et al. 2013).

4U 1636−53 is an Atoll LMXBs, consisting of a neutron star and a 0.4 $M_\odot$ companion in a 3.8 h orbit (Pedersen et al. 1982) at 6 kpc distance (Galloway et al. 2006). The source shows the full range of spectral states (Belloni et al. 2007; Altamirano et al. 2008). Highly coherent burst oscillations indicate that the system harbours a millisecond pulsar with a spin frequency of 581 Hz (Zhang et al. 1997; Strohmayer & Markwardt 2002). A pair of quasi-periodic oscillations (QPOs) at kHz frequencies were discovered by Zhang et al. (1996) and Wijnands et al. (1997). Kaaret et al. (1999) and de Avellar et al. (2013) found that the soft-X-ray emission in the lower kHz QPO (from the pair of kHz QPOs, the one at lower frequency) lags the hard-X-ray emission, suggesting that the emission is due to reprocessing of hard X-rays in a cooler Comptonizing corona or the accretion disc, in a region with a size of at most a few kilometres. In the last 10 yr, 4U 1636−53 showed a regular state transition cycle of ∼40 d (Shih et al. 2005; Belloni et al. 2007), making it an excellent source to study the variations of the broad-band spectrum and iron line as a function of spectral state.

In this work, we study the spectrum of 4U 1636−53 in different states. We use 11 observations from *Suzaku*, *XMM–Newton*, and the *Rossi X-Ray Timing Explorer* (*RXTE*) satellites covering a wide range in luminosity, allowing us to investigate the evolution of the different spectral components as a function of spectral state, and study possible correlations between the continuum spectrum and the iron line. Since the disc is illuminated and photon-ionized by the continuum emission to produce the iron line, correlations between the iron-line flux and the flux of different continuum components may provide an important clue to understand the origin of the iron emission line and the evolution of the accretion flow geometry.

2 OBSERVATIONS AND DATA REDUCTION

The data used in this work were collected by three satellites: five observations were made with *Suzaku*, while the other six were made simultaneously with the *XMM–Newton* and *RXTE* satellites. We call the *Suzaku* observations S1–S5 and the *XMM–Newton*/*RXTE* observations X1–X6, respectively. We provide details of all observations in Table 1.

We used all 16 s time-resolution Standard-2 data available from the *RXTE* Proportional Counter Array (PCA) from 1996 February 28 to 2011 September 18 to calculate two X-ray colours and the X-ray light curve. We defined the hard and soft colours as the 9.7–16.0/6.0–9.7 keV and the 3.5–6.0/2.0–3.5 keV count-rate ratios, and the intensity as the 2–16 keV count rate. We normalized the colours and intensity to those of the Crab nebula in observations taken close in time to the ones of 4U 1636−53 (see Zhang et al. 2009, for details of the procedure). We used the parameter S_a to indicate the approximate location of the source in the colour–colour diagram (see e.g. Méndez & van der Klis 1999; Zhang, Méndez & Altamirano 2011). We defined S_a as in Zhang et al. (2011), such that $S_a = 1$ corresponds to the top-right vertex and $S_a = 2$ to the bottom-left vertex of the colour–colour diagram. The coordinate of S_a is usually assumed to be a function of mass accretion rate (Hasinger & van der Klis 1989; Zhang et al. 2011). The S_a values of the 11 observations run from 1.33 to 2.23, with three observations (X1, X6, and S1) in the hard branch, $S_a < 2$, two observations (X4 and S2) in the soft branch, $S_a > 2$, and the rest clustered around the vertex between the two branches, $S_a \sim 2$. In Fig. 1, we show the colour–colour diagram, calculated as described above, for all *RXTE* observations of 4U 1636−53. We also plot there the curve that we used to define the S_a value of each observation. We also indicate there the approximate position of the source in the colour–colour diagram during the 11 observations analysed in this paper. In Fig. 2, we show part of the light curve of 4U 1636−53 obtained with the PCA detector on board *RXTE*. We show the 11 observations discussed in this paper following the same convention as in Fig. 1.

2.1 *Suzaku* data reduction

The *Suzaku* observations of 4U 1636−53 were carried out using two detectors: the X-ray Imaging Spectrometer (XIS) and the Hard X-ray Detector (HXD). The three XIS detectors cover the 0.2–12 keV energy range, with the two front-illuminated (FI) CCD detectors (XIS0, XIS3) being sensitive in the 0.4–12 keV range, while the back-illuminated (BI) CCD detector (XIS1) covers the 0.2–12 keV range. The HXD-PIN camera provides spectra in the 10–70 keV range. The 2 × 2 and 3 × 3 editing modes were applied to the XIS detectors with the 1/4 window mode and a burst option to limit the photon pile-up. For all five observations, the XIS-pointing position was applied. We list other details of the observations in Table 1.

Table 1. *Suzaku* and *XMM–Newton*/*RXTE* observations of 4U 1636−53.

Observation	Instrument	ObsID	Start date	Start time	Exposure (ks)[a]
S1	*Suzaku*	401050010	2007-02-09	09:18:22	22.3(FI); 11.1(BI); 20.3(HXD)
S2	*Suzaku*	401050020	2007-02-22	07:05:38	39.7(FI); 19.8(BI); 33.2(HXD)
S3	*Suzaku*	401050030	2007-03-01	01:01:07	38.2(FI); 19.1(BI); 45.2(HXD)
S4	*Suzaku*	401050040	2007-03-27	11:31:36	30.3(FI); 14.9(BI); 26.1(HXD)
S5	*Suzaku*	401050050	2007-03-29	11:19:47	9.8(FI); 4.9(BI); 11.0(HXD)
X1	*XMM–Newton*	0303250201	2005-08-29	18:24:23	25.7
	RXTE	91027-01-01-000		16:35:28	26.2 (PCA); 9.0 (HEXTE)
X2	*XMM–Newton*	0500350301	2007-09-28	15:44:56	14.3
	RXTE	93091-01-01-000		14:47:28	26.9 (PCA); 8.8 (HEXTE)
X3	*XMM–Newton*	0500350401	2008-02-27	04:15:37	34.7
	RXTE	93091-01-02-000		03:46:56	25.3 (PCA); 8.3 (HEXTE)
X4	*XMM–Newton*	0606070201	2009-03-25	22:59:30	23.8
	RXTE	94310-01-02-03		23:00:32	1.9 (PCA)
	RXTE	94310-01-02-04	2009-03-26	00:39:28	1.6 (PCA)
	RXTE	94310-01-02-05		02:17:36	1.4 (PCA)
	RXTE	94310-01-02-02		03:54:24	1.3 (PCA); 2.2 (HEXTE)
X5	*XMM–Newton*	0606070301	2009-09-05	01:57:03	32.8
	RXTE	94310-01-03-000		01:17:36	16.6 (PCA)
	RXTE	94310-01-03-00		08:20:32	7.3 (PCA); 7.6 (HEXTE)
X6	*XMM–Newton*	0606070401	2009-09-11	08:48:11	21.1
	RXTE	94310-01-04-00		08:42:24	18.4 (PCA); 5.7 (HEXTE)

[a]The final exposure time excludes X-ray bursts, background flares and instrument dropouts. The *XMM–Newton*/*RXTE* data are the same as those used by Sanna et al. (2013).

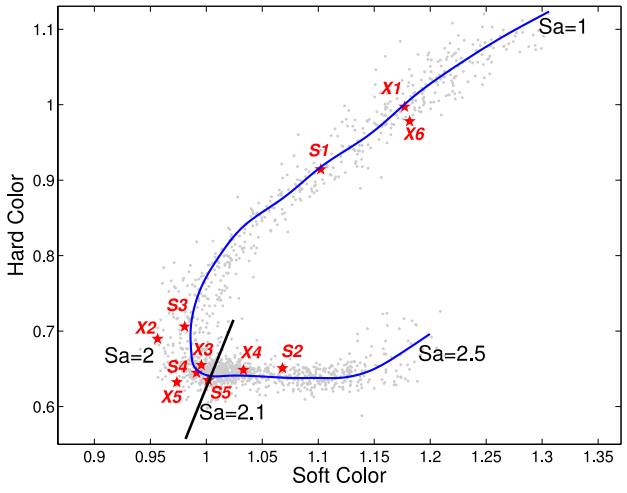

Figure 1. Colour–colour diagram of 4U 1636−53 using all *RXTE* observations (see the text). Each grey point represents the averaged Crab-normalized colours (see Zhang et al. 2011, for details) of a single *RXTE* observation. The red stars mark the position of the five *Suzaku* observations (S1–S5) and six *XMM–Newton*/*RXTE* observations (X1–X6). The position of the source in the diagram is parametrized by the length of the blue solid curve S_a. The diagonal black solid line indicates the position in the diagram for which $S_a = 2.1$ (see also Zhang et al. 2011).

All data reduction proceeded according to the *Suzaku* Data Reduction Guide.[1] We calibrated the XIS and HXD data using XIS CALDB 20111109 and HXD CALDB 20070710, respectively. We put together the 2 × 2 and 3 × 3 mode event files for each XIS detector into the HEASOFT tool XSELECT to produce good time intervals excluding X-ray bursts, and extracted spectra from a rectangular box region centred at the position of the source. We used the HEASOFT tools XISRMFGEN and XISSIMARFGEN to create the XIS redistribution matrix files and ancillary response files. We produced the final FI spectrum file by combining the spectra and responses of the XIS0 and the XIS3 data, while the final BI spectrum file was created from spectra and responses of the XIS1 data. We rebinned all the spectra to a minimum of 20 counts per bin. To test for pile-up, we extracted several spectra from the event files excluding a small rectangular area of different sizes within the rectangular region that we used previously to extract the spectrum of the source. We determined the optimal size of the inner rectangular area by checking that the model parameters of the spectral continuum did not change significantly when we increased the size of the inner rectangular area further. For the FI (BI) spectrum of observation S1, the width and the height of the inner rectangular area were, respectively, 43 and 54 (41 and 39) pixels. For the other four observations, we used the same width and height of the inner rectangular area for the FI and BI spectra, respectively, 77 and 103 pixels for S2 and S3, 88 and 88 pixels for S4, and 58 and 82 pixels for S5.

To produce the HXD-PIN spectra, we followed exactly the steps recommended by the *Suzaku* team. For each observation, the HXD-PIN data reduction process began with a clean event file. We extracted the PIN spectrum and applied the dead-time correction using the pseudo-events files. After we had extracted the non-X-ray background (NXB) spectrum, we increased the exposure time of the background spectrum by a factor of 10 since the NXB event file was calculated with a count rate 10 times higher than the real background count rate to reduce the statistical errors. Since the

[1] http://heasarc.nasa.gov/docs/suzaku/analysis/abc/

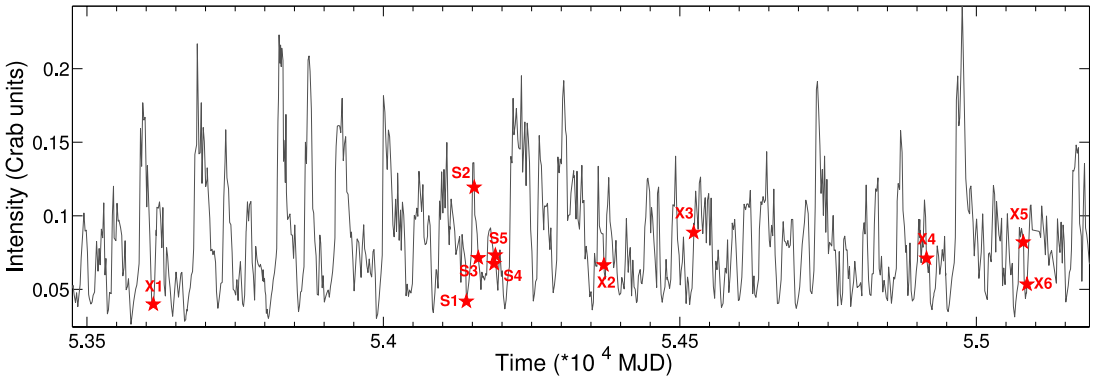

Figure 2. Long-term light curve of 4U 1636−53 obtained with the *RXTE*/PCA. For clarity, we only show the part of the light curve around the dates of the *XMM–Newton* and *Suzaku* observations. As in Fig. 1, the red stars mark the position of the five *Suzaku* observations (S1-S5) and six *XMM–Newton*/*RXTE* observations (X1-X6).

cosmic X-ray background was not included in the NXB event file, it was simulated and modelled (as a power law with a high energy cutoff component; see the *Suzaku* Data Reduction guide for details), and finally it was added to the NXB spectrum in order to provide the total background spectrum. As in the case of the XIS spectra, we excluded the time intervals with X-ray bursts to produce the X-ray spectra.

2.2 *XMM–Newton* and *RXTE* data reduction

In this paper, we used the same *XMM–Newton* and *RXTE* data as presented in Sanna et al. (2013). Details of the extraction and reduction process are given in Sanna et al. (2013). Here, we only summarize their steps. The six *XMM–Newton* observations used in this work were taken with the EPIC (European Photon Imaging Camera)-PN cameras in timing mode, in which one dimension of the CCDs is compressed to obtain a fast read out. The PN event files were processed using the tool `epproc` in SAS version 12.1. Intervals with X-ray bursts were excluded from the analysis, and all source spectra were rebinned to ensure there were at least 25 counts in every bin.

For the *RXTE* observations taken simultaneously with the *XMM–Newton* observations, Sanna et al. (2013) extracted spectra from the Standard 2 data taken with the third Proportional Counter Unit (PCU2), since it is the best calibrated detector, excluding intervals with X-ray bursts. A 0.6 per cent systematic error was added to the PCA data and the background spectrum was estimated using the tool PCABACKEST. The high energy X-ray timing experiment (HEXTE) spectrum was produced after excluding X-ray bursts, and no systematic errors were applied. For more details of the *XMM–Newton* and *RXTE* data reduction, we refer to Sanna et al. (2013).

3 SPECTRAL ANALYSIS

For each of the *Suzaku* observation, we fitted the XIS (0.9–10 keV) and HXD (10–30 keV) spectra together using XSPEC v12.8.0c. We ignored the energy range 1.5−2.5 keV due to problems in the calibration of the instrument (Ushio et al. 2009; Garson, Baring & Krawczynski 2010; Rivers et al. 2010). For the HXD spectrum, we selected the energy range below 30 keV since, for 4U 1636−53, that is the energy range where the source emission dominates over the background. The fits of the *XMM–Newton*/*RXTE* spectra were done using XSPEC v12.7.1 from 0.8 to 120 keV (PN: 0.8–11 keV; PCA: 10–25 keV; HEXTE: 20–120 keV; see Sanna et al. 2013).

For the *Suzaku* observations, we used the component PHABS to describe the photoelectric absorption in the interstellar medium, using the abundance table of Anders & Grevesse (1989) and the cross-section table of Balucinska-Church & McCammon (1992). In order to account for possible systematic errors in the cross-calibration between the different instruments, we included a constant factor in all the models. We fixed this constant factor to 1 for the FI and PN spectra in the *Suzaku* and *XMM–Newton* data, respectively, and we left it free for all the other spectra. For details of the *XMM–Newton* and *RXTE* spectral analysis, we refer to Sanna et al. (2013).

3.1 Spectral model

3.1.1 Continuum spectrum

We needed to include two thermal components and a Compotonized component to obtain a good fit to the continuum spectrum of all observations. We used a multicolour disc blackbody component, DISKBB (Mitsuda et al. 1984; Makishima et al. 1986), in XSPEC to describe the emission from the accretion disc, and a single temperature blackbody component, BBODY, to model the emission from the neutron-star surface and boundary layer. For the hard component, we used a thermally Comptonized continuum model, NTHCOMP (Zdziarski, Johnson & Magdziarz 1996; Życki, Done & Smith 1999). In this model, the source of the thermal seed photons for the Compton process can either come from the disc blackbody or the blackbody component. After some tests, we selected the former as the source of soft photons, the reason being that when we chose the blackbody as the source of seed photons, the fitting results showed that the blackbody component was no longer needed to fit the data (see also Sanna et al. 2013, for a similar situation regarding the fits to the *XMM–Newton*/*RXTE* data).

Previous works have shown that the parameters of the spectral components vary across the different spectral states. The temperatures of the thermal components is typically in the range of 0.5−2.0 keV in the soft state (Di Salvo et al. 2000a; Oosterbroek et al. 2001; Iaria et al. 2005), and below $\sim$ 1 keV in the hard state (Church & Balucińska-Church 2001; Barret, Olive & Oosterbroek 2003). The temperature of the corona changes in the opposite way, from 2 to 3 keV in the soft state to a few tens of keV in the hard state (e.g. Gierliński & Done 2003).

3.1.2 Iron-line model

The fits using only a continuum model revealed residuals around 6–7 keV, the energy range in which an iron emission line could in

principle be present, therefore, we also included in our models a component in that energy range to account for this putative line. We used, separately, four different models to fit the line (see Tables 4 and 5). First, we used a simple GUASS model to extract some general properties of the emission line, like the significance and the width. Since the resulting Gaussian line was in general broad (σ between ∼0.7 keV and ∼1.4 keV), we then also fitted the emission line with two relativistically broadened line models, DISKLINE (Fabian et al. 1989) and LAOR (Laor 1991), developed to describe the emission from a line emitted from an accretion disc around a non-rotating and maximally rotating black hole, respectively. Because of this last restriction, these two models may not be readily applicable to a moderately fast spinning neutron star. We therefore also used the KYRLINE model (Dovčiak et al. 2004) to fit the line, in which the line profile is calculated for the space–time around a black hole with arbitrary spin. In all cases, we constrained the energy of the line to the range 6.4−6.97 keV, corresponding to the energy of the Lyα line of neutral and H-like iron, respectively. For the DISKLINE, LAOR and KYRLINE models, we fixed the outer disc radius to $1000R_{\rm g}$, where $R_{\rm g} = GM/c^2$, with G being Newton's constant, c the speed of light, and M the mass of the neutron star. For the KYRLINE model, we did three separate fits with the spin parameter fixed at 0, 0.27 and 1, respectively (see Sanna et al. 2013, for details).

4 RESULTS

4.1 Fitting results

We give the best-fitting parameters to the *Suzaku* spectra of 4U 1636−53 in Tables 2 and 4. For completeness, we also reproduce here the results of Sanna et al. (2013) for the *XMM–Newton* and *RXTE* data (see Tables 3 and 5; unless otherwise indicated, all errors and upper limits correspond to the 90 per cent and 95 per cent confidence intervals for one parameter, respectively). We plot the evolution of the normalization of the blackbody component, $N_{\rm BB}$, and that of the disc blackbody, $N_{\rm DBB}$, in Fig. 3. The normalization of the blackbody component is proportional to $(R_{\rm NS+BL})^2$, where $R_{\rm NS+BL}$ is the apparent radius of the neutron star plus boundary layer (Gilfanov, Revnivtsev & Molkov 2003; White et al. 1988). The increase of the normalization of the BBODY component suggests that, as the source moves from the hard to the soft state, either the true emitting area on the surface of the neutron star increases or the colour-correction factor, which accounts for hardening of the spectrum arising from electron scattering in the neutron-star atmosphere and boundary layer (London, Taam & Howard 1986; Madej, Joss & Różańska 2004), decreases, or both. The DISKBB normalization is $N_{\rm DBB} \propto R_{\rm in}^2 \cos i/d^2$, where $R_{\rm in}$ is the radius of the inner edge of the accretion disc, i is the inclination of the disc with respect to the line of sight, and d is the distance to the source. Since d is constant, and assuming that the inclination angle of the accretion disc is the same in all observations, $\sqrt{N_{\rm DBB}} \propto R_{\rm in}$. Fig. 3 shows that the inferred inner radius of the disc decreases by a factor of ∼10 when the source evolves from the hard to the soft state, and in the soft state $R_{\rm in}$ remains more or less constant, suggesting that the disc may have reached the ISCO. The normalization of the NTHCOMP component (not plotted) shows no significant changes as a function of the source state.

In the soft state, the temperature of the inner disc is ∼0.6–0.8 keV, that of the neutron-star surface plus boundary layer is ∼1.7–2.0 keV, and the temperature of the corona is ∼2–8 keV. In the hard state, the temperature of the inner disc decreases to less than ∼0.5 keV, the temperature of the neutron-star surface plus boundary layer is ∼1.2–1.9 keV, while the temperature of the corona increases to ∼15–20 keV.

Combining the *Suzaku* results with those from the *XMM–Newton/RXTE* observations of Sanna et al. (2013), in Fig. 4, we show the evolution of these three temperatures and the photon index of the NTHCOMP component as a function of $S_{\rm a}$. The temperature at the inner disc radius increases significantly from ∼0.2 keV in the hard state to about 0.8 keV in the soft state (Fig. 4, upper panel), while the temperature of the blackbody increases slightly from ∼1.5 to ∼2 keV when $S_{\rm a}$ increases (Fig. 4, second panel from the top). The inner disc temperature evolution is consistent with the standard truncated disc scenario in neutron-star LMXBs (Done et al. 2007). When the source evolves from the hard to the soft state, mass accretion increases, the inner edge of the accretion disc moves towards the central compact object, and since the temperature in the disc is $T \propto \dot{M}^{1/4} R^{-3/4}$ (Shakura & Sunyaev 1973), the temperature at the inner edge of the disc increases. The increase of the (colour) temperature of the blackbody component could be due to either heating up of the surface of the neutron star plus boundary layer as $\dot{M}$ increases, or to a decreasing colour-correction factor, as the mass accretion rate on to the neutron star increases.

Moving from the hard to the soft state, the temperature of the corona (Fig. 4, third panel from the top) drops from ∼15 keV to less than ∼5 keV while Γ, the power-law index[2] of the NTHCOMP component (Fig. 4, bottom panel) remains more or less constant at around 2, or increases slightly, consistent with past measurement in other sources (e.g. Méndez et al. 1997). In the soft state, the thermal component dominates the emission below ∼20 keV, while in the hard state it is the Comptonized component that dominates the spectrum.

In Fig. 5, we show the residuals (in terms of sigmas) of all five *Suzaku* spectra when we fitted them with the continuum model described above plus a Gaussian line in the 6–7 keV range, with the normalization of the Gaussian line subsequently set to zero. We examined the significance of the line using the F-test for an extra parameter for the GUASS model of the line (see Protassov et al. 2002, for the applicability of the F-test in this case). The F-test probability for observations S1 to S5 is 0.0094, 0.0029, 1.1×10^{-7}, 0.0003, and 0.0086, respectively.

As we described in the previous section, since the Gaussian used to fit the line was always very broad, we also fitted the line with three different relativistically broadened components. (We note, however, that the fits with a Gaussian are good, and the fits with the relativistic line models are not significantly better than those with a Gaussian.) We found that, regardless of the model that we used to fit the line (DISKLINE, LAOR, or KYRLINE, the latter with the spin parameter fixed to either 0, 0.27 or 1), in most of the *Suzaku* observations the inclination angle and the emissivity index of the disc could not be well constrained. Considering this, we give the best-fitting parameters of the line for the different models in Table 4 (with the exception of the emissivity index, which was completely unconstrained in almost all fits), and we only describe the evolution of the inner disc radius and the flux of the line obtained from the fits. We notice that the best-fitting inclination angle in most cases is larger than ∼75°–80°. This value is inconsistent with the fact

[2] The power-law photon index of NTHCOMP, Γ, and the optical depth, τ, and electron temperature, kT_e, of the Compton corona are related through the equation $\Gamma = \sqrt{\frac{9}{4} + \frac{m_e c^2}{kT_e \tau(1+\tau/3)}} - \frac{1}{2}$ (Sunyaev & Titarchuk 1980; Zdziarski et al. 1996), where $m_{\rm e}$ is the electron mass and c the speed of light.

Table 2. *Suzaku* observations of 4U 1636−53 – parameters of the continuum components. The different columns correspond to the different models used to fit the iron line. The DISKBB normalization is $N_{\rm DBB} = (R_{\rm in}/d_{10})^2 \cos i$, with $R_{\rm in}$ the inner disc radius in km, d_{10} the distance to the source in units of 10 Kpc, and i the inclination of the accretion disc with respect to the line of sight. The BBODY normalization is $N_{\rm BB} = L_{39}/d_{10}^2$, with L_{39} the source luminosity in units of 10^{39} erg s^{-1} and d_{10} the same as for the DISKBB component. The NTHCOMP normalization is the flux density in photons cm^{-2} s^{-1} keV^{-1} at 1 keV.

	Model comp	Parameter	GAUSS	DISKLINE	LAOR	KYRLINE-0	KYRLINE-0.27	KYRLINE-1
S1 ($S_a = 1.54$)								
	PHABS	$N_{\rm H}(10^{22}{\rm cm}^{-2})$	0.23 ± 0.02	0.22 ± 0.02	0.23 ± 0.01	0.24 ± 0.02	0.23 ± 0.02	0.23 ± 0.01
	DISKBB	$kT_{\rm in}$(keV)	0.48 ± 0.07	$0.52^{+0.04}_{-0.07}$	0.48 ± 0.06	0.47 ± 0.07	0.48 ± 0.06	0.49 ± 0.05
		$N_{\rm DBB}(10^2)$	2.4 ± 0.5	2.2 ± 0.2	2.4 ± 0.3	2.5 ± 0.7	2.4 ± 0.4	2.4 ± 0.4
	BBODY	$kT_{\rm BB}$(keV)	1.5 ± 0.2	1.5 ± 0.1	1.5 ± 0.1	1.5 ± 0.2	1.5 ± 0.1	1.5 ± 0.2
		$N_{\rm BB}(10^{-3})$	1.5 ± 0.8	2.0 ± 0.6	1.5 ± 0.3	1.4 ± 0.6	1.6 ± 0.7	1.6 ± 0.5
	NTHCOMP	Γ	1.85 ± 0.75	1.82 ± 0.06	1.86 ± 0.05	1.86 ± 0.07	1.85 ± 0.07	1.84 ± 0.06
		kT_e(keV)	$13.1^{+12.8}_{-3.4}$	11.9 ± 3.3	13.7 ± 2.8	$13.3^{+13.7}_{-3.3}$	$13.0^{+10.6}_{-3.3}$	$12.8^{+6.8}_{-2.4}$
		$N_{\rm NTH}$	0.15 ± 0.03	0.13 ± 0.02	$0.151^{+0.005}_{-0.02}$	0.16 ± 0.04	0.15 ± 0.04	0.15 ± 0.03
	$\chi^2_\nu(\chi^2/{\rm d.o.f.})$		1.04 (655/627)	1.05 (655/625)	1.04 (651/625)	1.04 (652/625)	1.04 (652/625)	1.04 (653/625)
S2 ($S_a = 2.23$)								
	PHABS	$N_{\rm H}(10^{22}{\rm cm}^{-2})$	0.309 ± 0.007	0.305 ± 0.007	0.305 ± 0.005	0.304 ± 0.004	0.304 ± 0.004	0.304 ± 0.004
	DISKBB	$kT_{\rm in}$(keV)	0.68 ± 0.05	0.72 ± 0.03	0.73 ± 0.03	0.74 ± 0.03	0.74 ± 0.03	0.74 ± 0.02
		$N_{\rm DBB}(10^2)$	$0.5^{+1.8}_{-0.5}$	$1.4^{+0.5}_{-1.3}$	1.8 ± 0.7	1.8 ± 0.7	1.8 ± 0.4	1.7 ± 0.4
	BBODY	$kT_{\rm BB}$(keV)	$2.19^{+0.08}_{-0.3}$	$2.07^{+0.2}_{-0.06}$	1.9 ± 0.2	1.9 ± 0.3	1.9 ± 0.2	1.96 ± 0.06
		$N_{\rm BB}(10^{-3})$	$9.1^{+1.5}_{-3.8}$	8.3 ± 2.3	7.2 ± 1.9	7.3 ± 1.8	7.3 ± 1.6	7.5 ± 1.2
	NTHCOMP	Γ	2.6 ± 0.3	2.3 ± 0.4	2.2 ± 0.3	2.1 ± 0.4	2.1 ± 0.3	2.2 ± 0.2
		kT_e(keV)	4.3 ± 1.2	3.8 ± 1	3.5 ± 0.5	3.5 ± 0.4	3.5 ± 0.4	3.5 ± 0.3
		$N_{\rm NTH}$	$0.57^{+0.07}_{-0.2}$	0.42 ± 0.09	0.36 ± 0.09	0.34 ± 0.1	0.4 ± 0.1	0.36 ± 0.05
	$\chi^2_\nu(\chi^2/{\rm d.o.f.})$		1.17 (733/628)	1.17 (730/626)	1.17 (730/626)	1.16 (728/626)	1.16 (728/626)	1.16 (728/626)
S3 ($S_a = 1.98$)								
	PHABS	$N_{\rm H}(10^{22}{\rm cm}^{-2})$	0.292 ± 0.009	0.292 ± 0.005	0.296 ± 0.005	0.294 ± 0.007	0.294 ± 0.006	0.295 ± 0.006
	DISKBB	$kT_{\rm in}$(keV)	0.59 ± 0.05	0.59 ± 0.03	0.55 ± 0.02	0.57 ± 0.03	0.57 ± 0.03	0.57 ± 0.02
		$N_{\rm DBB}(10^2)$	$2.5^{+0.4}_{-0.9}$	2.5 ± 0.2	1.8 ± 0.3	2.2 ± 0.7	2.2 ± 0.7	2.3 ± 0.4
	BBODY	$kT_{\rm BB}$(keV)	2.0 ± 0.3	2.0 ± 0.1	2.3 ± 0.1	2.1 ± 0.3	2.1 ± 0.2	2.1 ± 0.2
		$N_{\rm BB}(10^{-3})$	$3.7^{+1.1}_{-0.6}$	3.7 ± 0.5	3.8 ± 0.3	3.6 ± 0.5	3.6 ± 0.5	3.6 ± 0.4
	NTHCOMP	Γ	2.2 ± 0.2	2.24 ± 0.07	$2.39^{+0.09}_{-0.01}$	2.3 ± 0.1	2.3 ± 0.1	2.30 ± 0.09
		kT_e(keV)	$7.6^{+5.1}_{-1.3}$	7.7 ± 1.1	$11.6^{+5.6}_{-2.0}$	$9.1^{+8.5}_{-1.9}$	$9.0^{+8.4}_{-1.4}$	$8.6^{+2.3}_{-1.2}$
		$N_{\rm NTH}$	0.3 ± 0.1	0.31 ± 0.07	0.39 ± 0.03	0.36 ± 0.1	0.36 ± 0.09	0.35 ± 0.07
	$\chi^2_\nu(\chi^2/{\rm d.o.f.})$		1.24 (780/628)	1.24 (774/626)	1.23 (771/626)	1.23 (773/626)	1.23 (773/626)	1.23 (773/626)
S4 ($S_a = 2.10$)								
	PHABS	$N_{\rm H}(10^{22}{\rm cm}^{-2})$	0.292 ± 0.009	0.289 ± 0.008	0.292 ± 0.006	0.291 ± 0.009	0.292 ± 0.008	0.292 ± 0.007
	DISKBB	$kT_{\rm in}$(keV)	0.70 ± 0.08	0.74 ± 0.04	0.71 ± 0.02	0.71 ± 0.05	0.70 ± 0.06	0.71 ± 0.06
		$N_{\rm DBB}(10^2)$	$1.5^{+0.6}_{-1.5}$	2.0 ± 0.5	$1.7^{+0.2}_{-1.1}$	$1.6^{+0.4}_{-1.2}$	$1.5^{+0.6}_{-1.1}$	$1.7^{+0.3}_{-0.9}$
	BBODY	$kT_{\rm BB}$(keV)	1.9 ± 0.3	1.7 ± 0.2	$1.88^{+0.2}_{-0.07}$	1.9 ± 0.2	1.9 ± 0.3	1.9 ± 0.2
		$N_{\rm BB}(10^{-3})$	$6.1^{+2.7}_{-1.2}$	$7.3^{+5.2}_{-1.8}$	6.3 ± 0.9	6.3 ± 1.1	6.3 ± 1.0	6.3 ± 1.5
	NTHCOMP	Γ	2.3 ± 0.6	2.0 ± 0.6	2.3 ± 0.2	2.3 ± 0.5	2.3 ± 0.4	2.2 ± 0.4
		kT_e(keV)	$4.4^{+3.9}_{-0.9}$	3.8 ± 0.8	4.2 ± 0.5	$4.3^{+2.4}_{-0.7}$	$4.4^{+2.4}_{-0.8}$	$4.2^{+1.7}_{-0.6}$
		$N_{\rm NTH}$	0.3 ± 0.2	$0.14^{+0.2}_{-0.13}$	$0.24^{+0.1}_{-0.05}$	$0.24^{+0.2}_{-0.08}$	0.3 ± 0.2	0.2 ± 0.1
	$\chi^2_\nu(\chi^2/{\rm d.o.f.})$		1.09 (807/740)	1.10 (810/738)	1.08 (800/738)	1.08 (799/738)	1.08 (799/738)	1.08 (799/738)
S5 ($S_a = 2.12$)								
	PHABS	$N_{\rm H}(10^{22}{\rm cm}^{-2})$	0.32 ± 0.01	0.32 ± 0.01	0.320 ± 0.006	0.32 ± 0.01	0.32 ± 0.01	0.32 ± 0.01
	DISKBB	$kT_{\rm in}$(keV)	$0.62^{+0.08}_{-0.02}$	0.61 ± 0.04	0.61 ± 0.03	0.61 ± 0.06	0.61 ± 0.06	0.61 ± 0.04
		$N_{\rm DBB}(10^2)$	<1.93	<1.56	<1.43	<2.00	< 2.00	< 1.64
	BBODY	$kT_{\rm BB}$(keV)	$2.11^{+0.09}_{-0.2}$	2.10 ± 0.07	2.12 ± 0.06	$2.10^{+0.08}_{-0.2}$	$2.10^{+0.09}_{-0.2}$	2.10 ± 0.08
		$N_{\rm BB}(10^{-3})$	$8.8^{+1.2}_{-2.8}$	8.8 ± 1.2	$8.8^{+1.2}_{-0.5}$	$8.9^{+1.1}_{-2.1}$	$8.9^{+1.1}_{-2.3}$	8.9 ± 1.3
	NTHCOMP	Γ	2.8 ± 0.3	2.8 ± 0.4	$2.78^{+0.14}_{-0.25}$	2.8 ± 0.5	2.8 ± 0.5	2.8 ± 0.3
		kT_e(keV)	$5.7^{+8.4}_{-3.5}$	$5.6^{+6.5}_{-1.7}$	$5.5^{+5.2}_{-0.8}$	$5.8^{+7.2}_{-1.8}$	$5.8^{+8.1}_{-3.4}$	$5.8^{+8.3}_{-1.7}$
		$N_{\rm NTH}$	$0.52^{+0.01}_{-0.3}$	$0.52^{+0.02}_{-0.1}$	$0.52^{+0.01}_{-0.2}$	$0.52^{+0.01}_{-0.3}$	$0.52^{+0.01}_{-0.3}$	0.52 ± 0.01
	$\chi^2_\nu(\chi^2/{\rm d.o.f.})$		1.04 (635/613)	1.04 (633/611)	1.03 (632/611)	1.03 (632/611)	1.03 (632/611)	1.03 (632/611)

that the source shows no dipping or eclipses, but it is similar to the inclination angle obtained by Pandel, Kaaret & Corbel (2008) and Sanna et al. (2013) from fits to the *XMM–Newton* spectra of 4U 1636−53.

In Fig. 6, we plot the normalization of the DISKBB component versus the inner disc radius deduced from the iron-line component for all observations of 4U 1636−53 and for the different models used to fit the iron line. The solid line in this plot is the best-fitting

Table 3. *XMM–Newton*/*RXTE* observations of 4U 1636−53 – parameters of the continuum components. The different columns correspond to the different models used to fit the iron line. The normalizations are the same as in Table 2.

	Model comp	Parameter	GAUSS	DISKLINE	LAOR	KYRLINE-0	KYRLINE-0.27	KYRLINE-1
X1 ($S_a = 1.33$)								
	PHABS	$N_H(10^{22}cm^{-2})$	0.42 ± 0.08	0.34 ± 0.07	0.4 ± 0.1	$0.41^{+0.06}_{-0.11}$	0.40 ± 0.09	0.47 ± 0.05
	DISKBB	kT_{in}(keV)	0.19 ± 0.03	0.18 ± 0.06	0.17 ± 0.02	0.18 ± 0.03	0.18 ± 0.03	0.20 ± 0.02
		$N_{DBB}(10^2)$	$166.5^{+159.9}_{-99.9}$	$112.4^{+185.3}_{-10}$	271 ± 189	$173.9^{+171.9}_{-113.2}$	$181.1^{+232.8}_{-113.4}$	$105.0^{+75.8}_{-58.6}$
	BBODY	kT_{BB}(keV)	$1.3^{+0.15}_{-0.06}$	1.56 ± 0.06	1.56 ± 0.09	1.56 ± 0.07	1.56 ± 0.07	1.56 ± 0.08
		$N_{BB}(10^{-3})$	0.9 ± 0.2	1.3 ± 0.2	1.1 ± 0.2	1.1 ± 0.2	1.1 ± 0.1	1.1 ± 0.1
	NTHCOMP	Γ	1.85 ± 0.02	1.84 ± 0.06	1.85 ± 0.01	1.85 ± 0.01	1.85 ± 0.01	1.86 ± 0.01
		kT_e(keV)	15.4 ± 1.2	15.2 ± 1.0	15.4 ± 1.2	15.4 ± 1.0	15.3 ± 1.1	15.5 ± 1.1
		N_{NTH}	0.198 ± 0.008	0.193 ± 0.006	0.201 ± 0.008	0.199 ± 0.006	0.198 ± 0.004	0.200 ± 0.004
	$\chi^2_\nu(\chi^2/\text{d.o.f.})$		1.08 (306/284)	1.18 (333/282)	1.09 (307/282)	1.11 (312/282)	1.11 (312/282)	1.12 (317/282)
X2 ($S_a = 2.01$)								
	PHABS	$N_H(10^{22}cm^{-2})$	0.30 ± 0.05	0.32 ± 0.02	0.31 ± 0.03	0.31 ± 0.03	0.31 ± 0.03	0.32 ± 0.03
	DISKBB	kT_{in}(keV)	0.65 ± 0.06	0.67 ± 0.02	0.65 ± 0.04	0.68 ± 0.04	0.67 ± 0.03	0.67 ± 0.04
		$N_{DBB}(10^2)$	1.1 ± 0.3	1.9 ± 0.2	1.3 ± 0.2	1.6 ± 0.2	1.7 ± 0.3	1.7 ± 0.2
	BBODY	kT_{BB}(keV)	1.76 ± 0.05	1.64 ± 0.03	1.75 ± 0.05	1.68 ± 0.05	1.68 ± 0.05	1.68 ± 0.04
		$N_{BB}(10^{-3})$	3.8 ± 0.7	6.1 ± 0.5	4.4 ± 0.2	5.3 ± 0.7	5.8 ± 0.6	5.8 ± 0.6
	NTHCOMP	Γ	2.3 ± 0.1	2.1 ± 0.2	2.3 ± 0.1	2.2 ± 0.2	2.2 ± 0.3	2.2 ± 0.2
		kT_e(keV)	6.1 ± 0.6	5.4 ± 0.2	6.2 ± 0.3	$5.6^{+1.4}_{-0.4}$	5.6 ± 0.5	5.6 ± 0.7
		N_{NTH}	0.29 ± 0.04	0.19 ± 0.02	0.27 ± 0.05	0.21 ± 0.04	0.21 ± 0.05	0.21 ± 0.04
	$\chi^2_\nu(\chi^2/\text{d.o.f.})$		1.05 (298/284)	1.07 (304/282)	1.06 (299/282)	1.07 (301/282)	1.07 (303/282)	1.07 (302/282)
X3 ($S_a = 2.08$)								
	PHABS	$N_H(10^{22}cm^{-2})$	0.30 ± 0.01	0.36 ± 0.06	0.36 ± 0.01	0.36 ± 0.01	0.37 ± 0.09	0.36 ± 0.03
	DISKBB	kT_{in}(keV)	0.79 ± 0.05	0.73 ± 0.01	0.71 ± 0.03	0.73 ± 0.02	0.73 ± 0.02	0.73 ± 0.04
		$N_{DBB}(10^2)$	$1.62^{+0.7}_{-0.03}$	2.37 ± 0.04	2.4 ± 0.5	2.45 ± 0.04	2.5 ± 0.4	2.4 ± 0.2
	BBODY	kT_{BB}(keV)	1.4 ± 0.3	1.48 ± 0.03	1.33 ± 0.07	1.46 ± 0.05	1.46 ± 0.04	1.46 ± 0.04
		$N_{BB}(10^{-3})$	6.9 ± 0.2	9.9 ± 0.3	$8.2^{+0.5}_{-2.1}$	$9.8^{+0.1}_{-1}$	10.4 ± 0.1	10.3 ± 0.6
	NTHCOMP	Γ	1.85 ± 0.04	1.82 ± 0.03	1.82 ± 0.02	$1.80^{+0.1}_{-0.03}$	1.7 ± 0.2	1.8 ± 0.2
		kT_e(keV)	3.3 ± 0.1	3.4 ± 0.1	3.2 ± 0.1	3.3 ± 0.1	3.3 ± 0.1	3.3 ± 0.7
		N_{NTH}	0.15 ± 0.01	0.13 ± 0.03	0.15 ± 0.02	0.13 ± 0.01	0.11 ± 0.01	0.11 ± 0.04
	$\chi^2_\nu(\chi^2/\text{d.o.f.})$		1.09 (306/281)	1.19 (333/279)	1.12 (314/279)	1.16 (325/279)	1.17 (326/279)	1.17 (328/279)
X4 ($S_a = 2.17$)								
	PHABS	$N_H(10^{22}cm^{-2})$	0.30 ± 0.01	0.30 ± 0.01	0.31 ± 0.02	0.30 ± 0.03	0.30 ± 0.01	0.30 ± 0.01
	DISKBB	kT_{in}(keV)	0.76 ± 0.03	0.77 ± 0.02	0.74 ± 0.02	0.78 ± 0.02	0.78 ± 0.03	0.78 ± 0.01
		$N_{DBB}(10^2)$	1.5 ± 0.1	1.42 ± 0.06	1.4 ± 0.1	$1.50^{+0.08}_{-0.04}$	1.53 ± 0.07	1.51 ± 0.08
	BBODY	kT_{BB}(keV)	1.67 ± 0.03	$1.73^{+0.02}_{-0.08}$	1.72 ± 0.04	1.70 ± 0.02	1.70 ± 0.02	1.71 ± 0.02
		$N_{BB}(10^{-3})$	8.6 ± 2.1	9.3 ± 1.3	7.8 ± 0.9	9.6 ± 1.6	10.1 ± 1.3	$10.1^{+1.3}_{-3.1}$
	NTHCOMP	Γ	1.9 ± 0.2	2.0 ± 0.2	2.1 ± 0.3	1.9 ± 0.3	1.8 ± 0.3	1.8 ± 0.3
		kT_e(keV)	$3.8^{+1.3}_{-0.2}$	4.2 ± 0.2	4.1 ± 0.2	4.0 ± 0.2	3.9 ± 0.2	$4.0^{+1.7}_{-0.2}$
		N_{NTH}	0.10 ± 0.02	0.09 ± 0.01	0.14 ± 0.03	0.07 ± 0.01	0.06 ± 0.01	0.06 ± 0.02
	$\chi^2_\nu(\chi^2/\text{d.o.f.})$		1.08 (304/281)	1.06 (297/279)	1.09 (304/279)	1.06 (295/279)	1.06 (296/279)	1.06 (296/279)
X5 ($S_a = 2.09$)								
	PHABS	$N_H(10^{22}cm^{-2})$	0.28 ± 0.02	0.30 ± 0.02	0.29 ± 0.03	0.29 ± 0.02	0.29 ± 0.01	0.29 ± 0.01
	DISKBB	kT_{in}(keV)	0.75 ± 0.04	0.75 ± 0.01	0.73 ± 0.02	0.79 ± 0.02	0.79 ± 0.02	0.79 ± 0.04
		$N_{DBB}(10^2)$	0.7 ± 0.3	1.46 ± 0.09	1.20 ± 0.12	1.46 ± 0.09	1.54 ± 0.09	1.5 ± 0.2
	BBODY	kT_{BB}(keV)	2.0 ± 0.1	1.68 ± 0.02	$1.67^{+0.04}_{-0.17}$	1.63 ± 0.03	1.63 ± 0.02	1.64 ± 0.03
		$N_{BB}(10^{-3})$	4.9 ± 0.5	$6.7^{+1.6}_{-0.2}$	4.4 ± 0.7	7.4 ± 1.1	7.7 ± 1.3	$7.4^{+4}_{-0.4}$
	NTHCOMP	Γ	2.4 ± 0.2	2.0 ± 0.1	2.1 ± 0.1	1.9 ± 0.2	1.8 ± 0.1	1.9 ± 0.1
		kT_e(keV)	4.2 ± 0.8	$3.6^{+0.1}_{-0.8}$	$3.4^{+0.8}_{-0.1}$	$3.5^{+0.2}_{-0.7}$	3.4 ± 0.1	3.5 ± 0.1
		N_{NTH}	$0.29^{+0.1}_{-0.04}$	0.18 ± 0.03	0.23 ± 0.02	0.12 ± 0.01	0.11 ± 0.02	0.12 ± 0.01
	$\chi^2_\nu(\chi^2/\text{d.o.f.})$		1.12 (304/272)	1.22 (331/270)	1.15 (310/270)	1.17 (317/270)	1.18 (320/270)	1.21 (327/270)
X6 ($S_a = 1.36$)								
	PHABS	$N_H(10^{22}cm^{-2})$	0.32 ± 0.05	$0.27^{+0.03}_{-0.09}$	0.32 ± 0.07	0.31 ± 0.05	0.31 ± 0.06	0.29 ± 0.05
	DISKBB	kT_{in}(keV)	0.32 ± 0.05	0.41 ± 0.03	0.33 ± 0.06	0.34 ± 0.05	0.35 ± 0.05	0.37 ± 0.05
		$N_{DBB}(10^2)$	$7.1^{+4.7}_{-2.5}$	$3.6^{+1.9}_{-0.3}$	$6.4^{+4.4}_{-1.2}$	$6.1^{+2.2}_{-0.5}$	$5.8^{+4.2}_{-1.1}$	$4.7^{+6}_{-0.7}$
	BBODY	kT_{BB}(keV)	1.8 ± 0.1	$1.73^{+0.04}_{-0.1}$	1.9 ± 0.1	1.89 ± 0.08	1.88 ± 0.02	1.86 ± 0.08
		$N_{BB}(10^{-3})$	1.7 ± 0.3	2.5 ± 0.3	1.8 ± 0.2	2.2 ± 0.1	2.2 ± 0.2	2.2 ± 0.2
	NTHCOMP	Γ	1.9 ± 0.1	1.9 ± 0.1	1.9 ± 0.2	1.9 ± 0.1	1.9 ± 0.1	1.9 ± 0.1
		kT_e(keV)	$15.7^{+4.2}_{-2.6}$	14.5 ± 1.8	$16.8^{+5}_{-2.8}$	$16.8^{+4.2}_{-3}$	$16.5^{+4.5}_{-2.7}$	$16.2^{+3.8}_{-2.7}$
		N_{NTH}	0.23 ± 0.02	0.19 ± 0.01	0.23 ± 0.02	0.22 ± 0.02	0.22 ± 0.02	0.21 ± 0.01
	$\chi^2_\nu(\chi^2/\text{d.o.f.})$		0.93 (259/278)	1.06 (291/276)	0.94 (260/276)	0.97 (268/276)	0.97 (268/276)	0.98 (270/276)

Table 4. *Suzaku* observations of 4U 1636−53 – parameters of the Fe line[a] for the different models used to fit the line. In all cases, the line normalization is given in units of photons cm^{-2} s^{-1}.

	E_{line}(keV)	σ(keV)	$i(^\circ)$	$R_{in}(R_g)$	Normalization(10^{-3})	$\chi^2_\nu(\chi^2/d.o.f.)$
S1 ($S_a = 1.54$)						
GAUSS	$6.40^{+0.26}_{-0}$	0.8±0.4	–		$0.7^{+0.8}_{-0.5}$	1.04 (655/627)
DISKLINE	$6.40^{+0.31}_{-0}$	–	$44.9^{+45.1}_{-9.7}$	$7.5^{+57.5}_{-1.5}$	$0.4^{+0.4}_{-0.2}$	1.05 (655/625)
LAOR	$6.49^{+0.10}_{-0.09}$	–	86.3 ±0.3	$19.9^{+11.2}_{-3.3}$	$0.7^{+0.3}_{-0.2}$	1.04 (651/625)
KYR-0	$6.40^{+0.19}_{-0}$	–	$86.2^{+2.8}_{-11.8}$	17.5±10.5	$0.7^{+0.4}_{-0.3}$	1.04 (652/625)
KYR-0.27	$6.52^{+0.05}_{-0.12}$	–	$87.6^{+1.3}_{-14.9}$	$26.4^{+3.7}_{-13.2}$	0.6±0.2	1.04 (652/625)
KYR-1	$6.54^{+0.20}_{-0.14}$	–	$87.6^{+1.3}_{-57.0}$	$26.8^{+3.9}_{-16.1}$	$0.6^{+0.4}_{-0.1}$	1.04 (653/625)
S2 ($S_a = 2.23$)						
GAUSS	$6.40^{+0.08}_{-0}$	0.8 ±0.3	–	–	$1.3^{+0.9}_{-0.8}$	1.17 (733/628)
DISKLINE	$6.97^{+0}_{-0.35}$	–	23.8 ±5.0	$6.8^{+2.8}_{-0.8}$	0.9±0.5	1.17 (730/626)
LAOR	6.50 ±0.06	–	$0.01^{+13.2}_{-0.01}$	$5.0^{+11.1}_{-3.7}$	0.5±0.4	1.17 (730/626)
KYR-0	$6.40^{+0.30}_{-0}$	–	$28.2^{+1.3}_{-5.3}$	$11.8^{+0.9}_{-2.4}$	0.6±0.2	1.16 (728/626)
KYR-0.27	$6.42^{+0.36}_{-0.02}$	–	$27.8^{+1.7}_{-3.8}$	$11.4^{+1.3}_{-5.0}$	0.6±0.2	1.16 (728/626)
KYR-1	$6.40^{+0.23}_{-0}$	–	$28.3^{+1.2}_{-5.2}$	11.3±1.3	0.6±0.2	1.16 (728/626)
S3 ($S_a = 1.98$)						
GAUSS	$6.61^{+0.17}_{-0.21}$	0.8 ±0.2	–	–	$1.4^{+1.4}_{-0.7}$	1.24 (780/628)
DISKLINE	$6.43^{+0.12}_{-0.03}$	–	$79.3^{+10.7}_{-20.9}$	12.0±5.0	1.4±0.4	1.24 (774/626)
LAOR	$6.44^{+0.11}_{-0.04}$	–	86.4 ±0.2	$11.25^{+1.7}_{-0.07}$	2.3±0.4	1.23 (771/626)
KYR-0	$6.40^{+0.13}_{-0}$	–	$85.3^{+1.9}_{-10.7}$	$11.9^{+2.8}_{-1.7}$	$1.9^{+0.6}_{-0.3}$	1.23 (773/626)
KYR-0.27	$6.40^{+0.13}_{-0}$	–	$85.1^{+1.8}_{-5.5}$	11.8±2.5	1.9±0.7	1.23 (773/626)
KYR-1	$6.44^{+0.12}_{-0.04}$	–	$83.9^{+2.5}_{-8.5}$	11.8±2.8	1.8±0.5	1.23 (773/626)
S4 ($S_a = 2.10$)						
GAUSS	$6.40^{+0.18}_{-0}$	1.04 ±0.25	–	–	2.3 ±1.4	1.09 (807/740)
DISKLINE	$6.40^{+0.17}_{-0}$	–	$90.0^{+0}_{-28.4}$	$12.4^{+8.6}_{-6.4}$	1.2 ±0.5	1.10 (810/738)
LAOR	$6.55^{+0.07}_{-0.11}$	–	86.26 ±0.2	16.1 ±3.4	1.6 ±0.4	1.08 (800/738)
KYR-0	$6.46^{+0.13}_{-0.06}$	–	86.9 ±1.5	$15.5^{+4.8}_{-1.3}$	1.8 ±0.3	1.08 (799/738)
KYR-0.27	$6.47^{+0.13}_{-0.07}$	–	86.8 ±1.5	$15.5^{+5.0}_{-2.5}$	1.8 ±0.4	1.08 (799/738)
KYR-1	$6.55^{+0.09}_{-0.12}$	–	86.1 ±1.5	18.0 ±3.9	1.6 ±0.5	1.08 (799/738)
S5 ($S_a = 2.12$)						
GAUSS	$6.40^{+0.20}_{-0}$	0.7 ±0.3	–	–	1.4 ±0.8	1.04 (635/613)
DISKLINE	$6.40^{+0.23}_{-0}$	–	$76.2^{+13.8}_{-22.7}$	$26.9^{+12.7}_{-18.2}$	1.2 ±0.4	1.04 (633/611)
LAOR	$6.40^{+0.26}_{-0}$	–	$86.2^{+2.8}_{-13.4}$	$32.4^{+10.8}_{-24.6}$	1.3 ±0.3	1.03 (632/611)
KYR-0	$6.41^{+0.04}_{-0.01}$	–	86.3 ±2.5	$37.2^{+852.7}_{-15.2}$	1.2 ±0.4	1.03 (632/611)
KYR-0.27	$6.42^{+0.04}_{-0.02}$	–	86.3 ±2.5	$37.2^{+800.1}_{-15.4}$	1.2 ±0.4	1.03 (632/611)
KYR-1	$6.42^{+0.05}_{-0.02}$	–	86.3 ±2.5	$37.0^{+258.7}_{-16.0}$	1.2 ±0.4	1.03 (632/611)

[a]Although it was left free during the fits, we do not give the emissivity index in this (and the next table) because in almost all fits this parameter was completely unconstrained. The errors in all the other parameters were calculated leaving the emissivity index free.

quadratic relation to the data (all models of the line together), $N_{dbb} = C \times R^2_{in}$. From this figure, it is apparent that the normalization of the DISKBB component and the inner disc radius deduced from the iron-line profile do not follow the expected relation.

4.2 Flux evolution

As shown in Fig. 7, the 0.5–130 keV unabsorbed flux (continuum+line) of the 11 observations remains more or less constant, or increases slightly, as a function of S_a. From Fig. 8, it is apparent that the flux of the blackbody (upper panel) and the disc components (middle panel) both increase with S_a. The NTHCOMP flux (lower panel) remains more or less constant across the whole S_a range. As shown in Fig. 9, the flux of the iron line behaves in a complex way as a function of the S_a. The line flux initially decreases slightly as S_a increases, and it then shows a large scatter at around $S_a = 2.1$, close to the position of the vertex in the colour–colour diagram (see Fig. 1).

We also studied the correlation between the flux and the equivalent width of the iron line and the two possible illuminating components, either the Comptonizing corona (Fig. 10) or the neutron-star surface plus boundary layer. Both panels of Fig. 10 show that, for

Table 5. *XMM–Newton/RXTE* observations of 4U 1636−53 – parameters of the Fe line, for the different models used to fit the line. In all cases, the line normalization is given in units of photons cm^{-2} s^{-1}.

	E_{line}(keV)	σ(keV)	$i(^\circ)$	$R_{in}(R_g)$	Normalization(10^{-3})	$\chi^2_\nu(\chi^2/d.o.f.)$
X1 ($S_a = 1.33$)						
GAUSS	$6.40^{+0.07}_{-0}$	1.27 ±0.12	–	–	4.2±0.9	1.08 (306/284)
DISKLINE	$6.40^{+0.02}_{-0}$	–	$90.0^{+0}_{-15.9}$	$10.6^{+1.5}_{-2.6}$	2.1±0.2	1.18 (333/282)
LAOR	$6.44^{+0.08}_{-0.04}$	–	86.3 ±0.2	$10.8^{+0.6}_{-2.9}$	2.5±0.4	1.09 (307/282)
KYR-0	$6.40^{+0.06}_{-0}$	–	86.1 ±0.8	10.8±1.7	2.4±0.3	1.11 (312/282)
KYR-0.27	$6.40^{+0.06}_{-0}$	–	85.9 ±0.8	$10.6^{+1.9}_{-1.2}$	2.4±0.3	1.11 (312/282)
KYR-1	$6.40^{+0.06}_{-0}$	–	85.1 ±0.9	$9.9^{+1.9}_{-1.1}$	2.5±0.3	1.12 (317/282)
X2 ($S_a = 2.01$)						
GAUSS	$6.40^{+0.07}_{-0}$	1.3 ±0.1	–	–	7.6±1.6	1.05 (298/284)
DISKLINE	$6.40^{+0.07}_{-0}$	–	$72.5^{+17.5}_{-11.7}$	$10.7^{+4.5}_{-2.4}$	3.2±0.5	1.07 (304/282)
LAOR	$6.40^{+0.24}_{-0}$	–	$86.8^{+3.2}_{-0.4}$	$4.0^{+5.6}_{-0.8}$	6.4±0.1	1.06 (299/282)
KYR-0	$6.4^{+0.2}_{-0}$	–	88.9 ±1.0	$6.3^{+1.1}_{-0.3}$	5.3±0.8	1.07 (301/282)
KYR-0.27	$6.4^{+0.1}_{-0}$	–	$83.9^{+2.1}_{-7.9}$	12.5±2.5	$3.6^{+2}_{-0.6}$	1.07 (303/282)
KYR-1	$6.4^{+0.1}_{-0}$	–	$83.0^{+2.1}_{-5.8}$	$11.8^{+3.2}_{-1.7}$	3.6±0.5	1.07 (302/282)
X3 ($S_a = 2.08$)						
GAUSS	$6.40^{+0.06}_{-0}$	1.4±0.1	–	–	11.7 ±0.7	1.09 (306/281)
DISKLINE	$6.40^{+0.03}_{-0}$	–	$90.0^{+0}_{-15.9}$	$8.4^{+0.7}_{-1.5}$	4.6 ±0.4	1.19 (333/279)
LAOR	$6.40^{+0.05}_{-0}$	–	$87.5^{+2.5}_{-0.5}$	2.3 ±0.4	$9.6^{+0.5}_{-1}$	1.12 (314/279)
KYR-0	6.67 ±0.07	–	86.2 ±0.7	13.1±1.3	4.4±0.4	1.16 (325/279)
KYR-0.27	6.68 ±0.07	–	86.1 ±0.8	13.1±1.4	4.3±0.4	1.17 (326/279)
KYR-1	6.7 ±0.1	–	$85.6^{+2.1}_{-5.8}$	$12.9^{+3.2}_{-1.7}$	4.3±0.5	1.17 (328/279)
X4 ($S_a = 2.17$)						
GAUSS	6.86 ±0.11	1 ±0.2	–	–	2.9±1.0	1.08 (304/281)
DISKLINE	$6.43^{+0.05}_{-0.03}$	–	73.4 ±5.3	$6.0^{+2.8}_{-0}$	$2.6^{+1.0}_{-0.4}$	1.06 (297/279)
LAOR	$6.72^{+0.15}_{-0.32}$	–	88.1 ±1.9	$2.8^{+1.2}_{-0.8}$	3.5±0.1	1.09 (304/279)
KYR-0	$6.43^{+0.1}_{-0.03}$	–	$72.3^{+9.2}_{-4.9}$	$6.0^{+1.9}_{-0}$	2.4±0.6	1.06 (295/279)
KYR-0.27	$6.43^{+0.07}_{-0.03}$	–	$72.1^{+9.2}_{-5.2}$	$5.7^{+2}_{-0.6}$	2.4±0.5	1.06 (296/279)
KYR-1	$6.44^{+0.07}_{-0.04}$	–	74.3 ±6.5	5.3 ±1.6	2.3±0.5	1.06 (296/279)
X5 ($S_a = 2.09$)						
GAUSS	$6.41^{+0.09}_{-0.01}$	1.4±0.1	–	–	$8.6^{+1.8}_{-1}$	1.12 (304/272)
DISKLINE	$6.40^{+0.02}_{-0}$	–	$89.9^{+0.1}_{-14.5}$	$6.5^{+0.6}_{-0.5}$	3.8±0.5	1.22 (331/270)
LAOR	$6.40^{+0.06}_{-0}$	–	$90.0^{+0}_{-1.7}$	$2.0^{+0.4}_{-0.2}$	6.1±0.7	1.15 (310/270)
KYR-0	$6.40^{+0.04}_{-0}$	–	87 ±1	$6.2^{+0.4}_{-0.2}$	4.6±0.5	1.17 (317/270)
KYR-0.27	$6.40^{+0.04}_{-0}$	–	86.7 ±1.5	5.9 ±0.6	4.5±0.6	1.18 (320/270)
KYR-1	$6.40^{+0.03}_{-0}$	–	$89.0^{+1}_{-1.3}$	2.6 ±0.1	5.4±0.6	1.21 (327/270)
X6 ($S_a = 1.36$)						
GAUSS	$6.40^{+0.05}_{-0}$	1.2±0.1	–	–	4 ±1	0.93 (259/278)
DISKLINE	$6.40^{+0.02}_{-0}$	–	$90.0^{+0}_{-21.5}$	$8.0^{+6.3}_{-2}$	$2.4^{+0.3}_{-0.7}$	1.06 (291/276)
LAOR	$6.40^{+0.07}_{-0}$	–	86.4 ±0.2	6.2 ±1.9	3.7 ±0.6	0.94 (260/276)
KYR-0	$6.40^{+0.07}_{-0}$	–	86.8 ±0.8	$12.2^{+1.9}_{-2.6}$	2.6 ±0.3	0.97 (268/276)
KYR-0.27	$6.40^{+0.07}_{-0}$	–	86.5 ±0.8	$12.2^{+1.7}_{-2.6}$	2.5 ±0.3	0.97 (268/276)
KYR-1	$6.40^{+0.09}_{-0}$	–	86 ±1	12.1±2.1	2.5 ±0.3	0.98 (270/276)

the fits of the line with the GUASS model, there is a strong positive correlation between, respectively, the flux and equivalent width of the line and the flux of NTHCOMP when the NTHCOMP flux is below $\sim 15 \times 10^{-10}$ erg cm^{-2} s^{-1}, and an anticorrelation above that value. For the fit of the line with the KYRLINE model there is a weak positive correlation between the flux of the line and the flux of the NTHCOMP component when the NTHCOMP flux is below $\sim 15 \times 10^{-10}$ erg cm^{-2} s^{-1}, and a strong anticorrelation above that value. For clarity reasons, in both panels of this figure, we only plot the results of the line fits with the GUASS and KYRLINE, spin

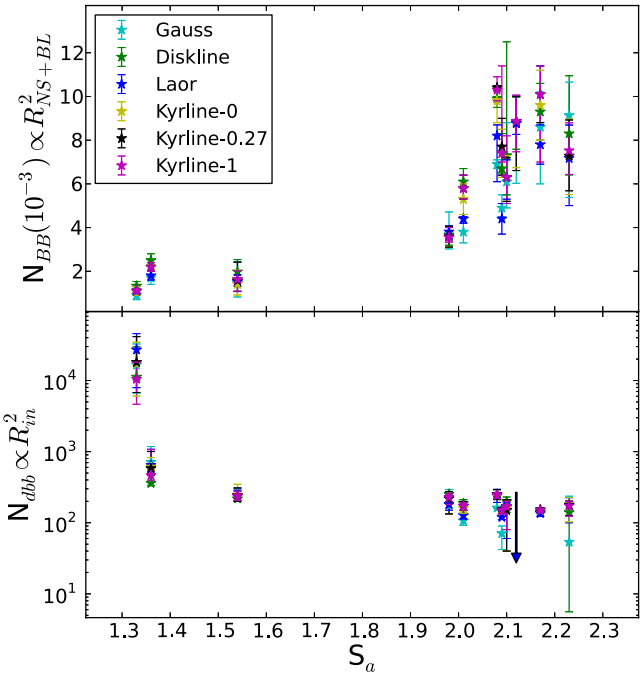

Figure 3. Normalization of the blackbody (upper panel) and disc blackbody (lower panel) components in 4U 1636−53 as a function of S_a for the five *Suzaku* and six *XMM–Newton*/*RXTE* observations. Different colours show the results of fits with different models to the iron line, as indicated in the legend, with Kyrline-0, Kyrline-0.27 and Kyrline-1 representing the results when we fitted the line with a KYRLINE model with the spin parameter fixed to 0, 0.27 or 1, respectively. The blue arrow in the lower panel shows the upper limit of the normalization in observation S5 where we did not significantly detect emission from the disc.

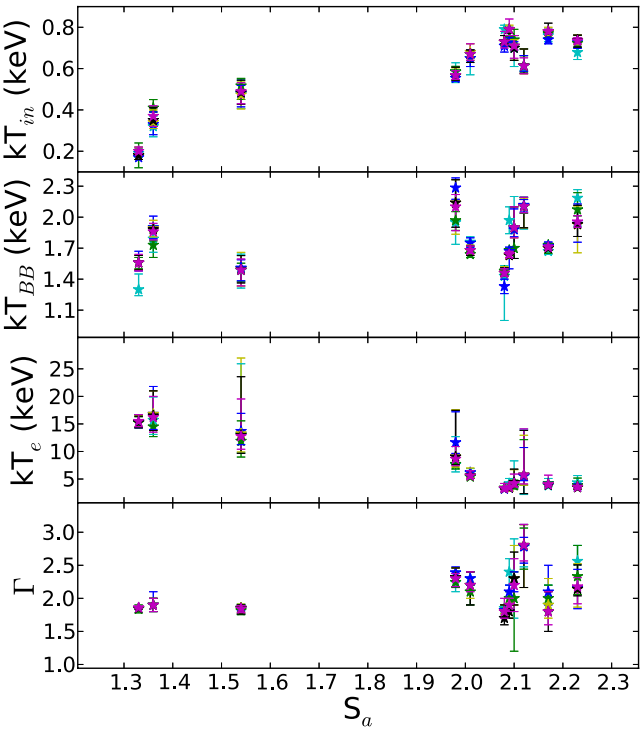

Figure 4. Temperature of the DISKBB (upper panel) BBODY (second panel from the top) components, electron temperature (third panel from the top) and power-law index Γ (lower panel) of the NTHCOMP component in 4U 1636−53 as a function of S_a. Symbols are the same as in Fig. 3.

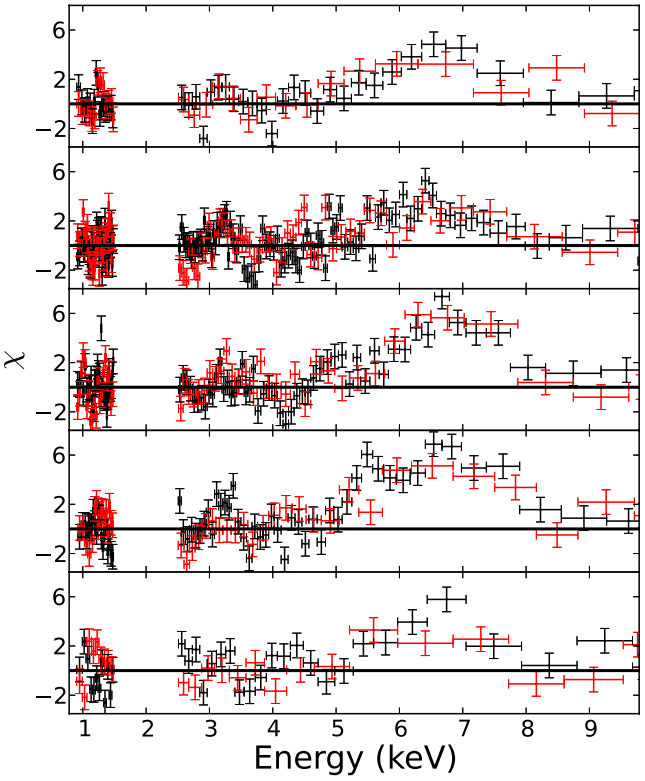

Figure 5. Residuals in terms of sigmas for the 5 *Suzaku* observations of 4U 1636−53 for the continuum model described in the text plus a Gaussian line, after we set the normalization of the GUASS component in the best-fitting model to zero. From top to bottom, the plots correspond to the observation S1-S5. The residuals of the FI and BI spectrum are rebinned and plotted in black and red, respectively.

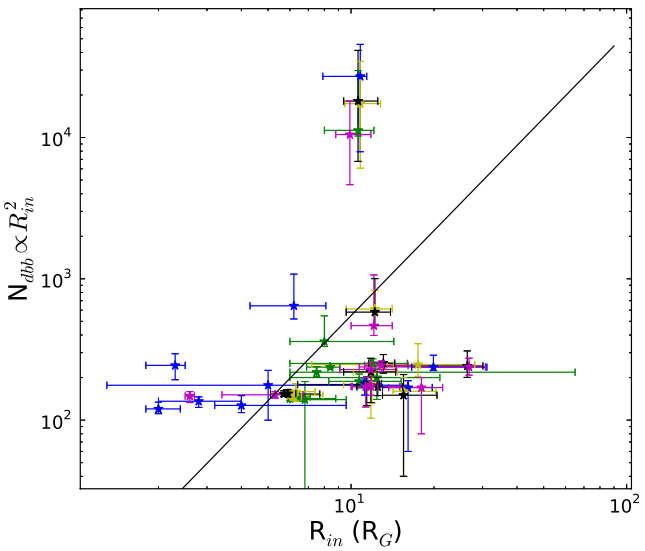

Figure 6. Normalization of the DISKBB component versus the inner disc radius deduced from the iron-line component for all observations of 4U 1636−53. The black solid line shows the best-fitting result when a quadratic relation $N_{\rm dbb} = C \times R^2_{\rm in}$ is fitted to the data. We do not include observation S5 since for that observation the normalization of DISKBB is consistent with zero. Symbols are the same as in Fig. 3.

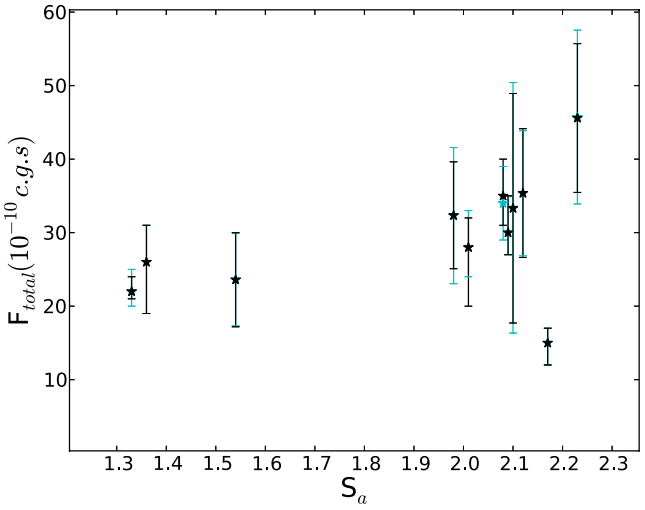

Figure 7. Total unabsorbed flux in the 0.5–130 keV range of 4U 1636−53 as a function of S_a. Symbols are the same as in Fig. 3. For clarity, we only plot the GUASS and KYRLINE-0.27 results here. The other models of the line give consistent results.

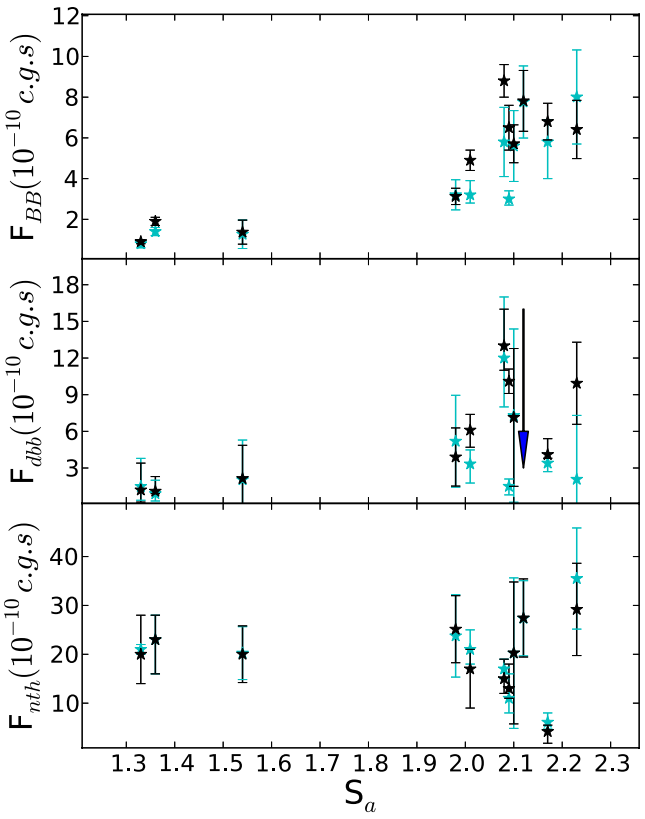

Figure 8. Unabsorbed flux for the blackbody and disc blackbody component (upper and middle panels, respectively) in the 0.5–130 keV range for 4U 1636−53 as a function of S_a. The blue arrow in the second panel shows the upper limit of the flux in observation S5 where we did not significantly detect emission from the disc. The lower panel shows the unabsorbed 0.5–130 keV flux of the NTHCOMP component in 4U 1636−53 as a function of S_a. Symbols are the same as in Fig. 3. For clarity, we only plot the GAUSS and KYRLINE-0.27 results here. The other models of the line give consistent results.

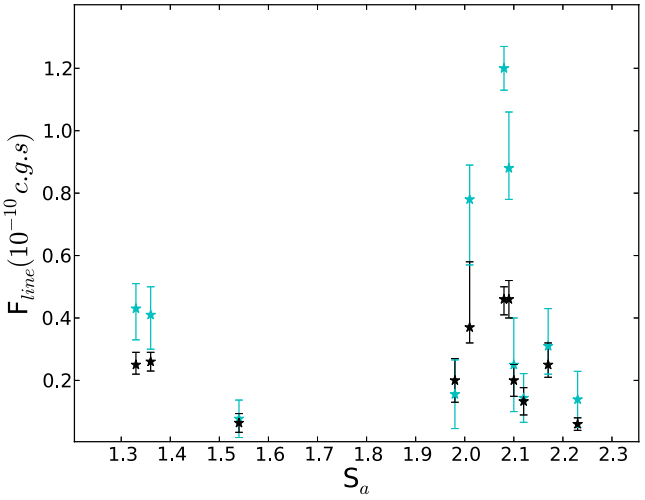

Figure 9. Unabsorbed iron-line flux in the 0.5–130 keV range for 4U 1636−53 versus S_a. Symbols are the same as in Fig. 3. For clarity, we only plot the GUASS and KYRLINE-0.27 results here. The other models of the line give consistent results.

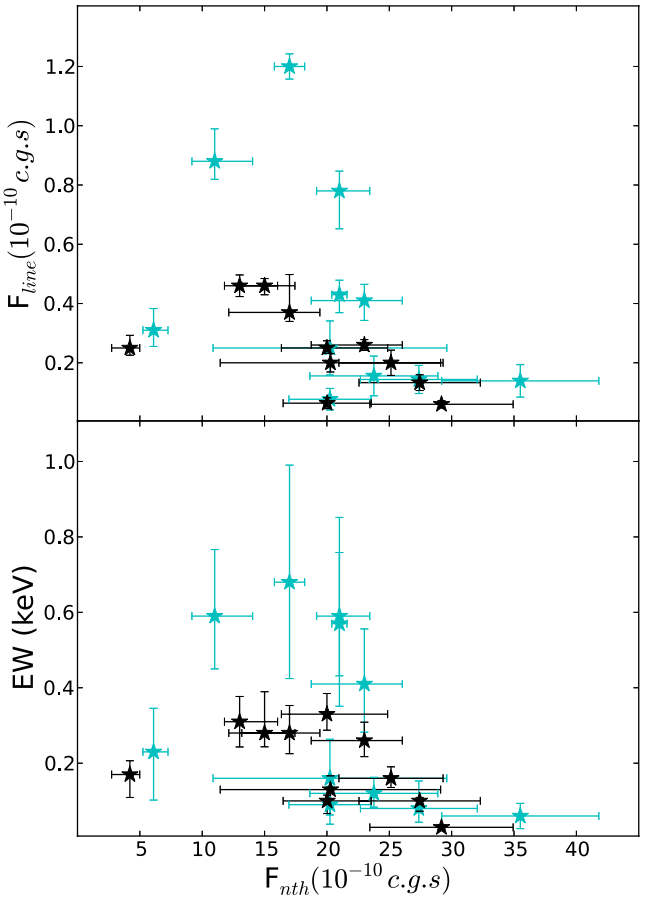

Figure 10. Flux (0.5–130 keV; upper panel) and equivalent width (lower panel) of the iron line versus the flux (0.5–130 keV) of the NTHCOMP continuum component in 4U 1636−53. For clarity, we only plot the results of GUASS (in cyan) and KYRLINE-0.27 (in black) here. The other models of the line give consistent results. For this figure, we use the 1σ errors in the flux and equivalent width.

parameter 0.27, models. For both panels, the fits with the LAOR model give results consistent with those of the GUASS model, while the results for the fits with DISKLINE and KYRLINE with spins of 0 and 1 are consistent with those of the KYRLINE with spin 0.27 shown in the figure. The maximum in this plot happens when the source is at $S_a \approx 2.1$, close to the vertex in the colour–colour diagram. The flux and equivalent width of the line do not appear to be correlated with the flux of the BBODY component (not plotted). Given that the ionizing photons that produce the iron line must have energies above ∼7 keV, we also compared the flux and equivalent width of the iron line versus the 7−130 keV flux of the BBODY and NTHCOMP components. The results (not plotted) are similar to those for the full energy range. The flux and equivalent width of the line first increase and then decrease as the 7−130 keV flux of the NTHCOMP component increases, but are not correlated with the 7−130 keV flux of the BBODY component.

5 DISCUSSION

We used all available *Suzaku* and *XMM–Newton* observations, the latter complemented with simultaneous *RXTE* observations, to study the evolution of the continuum spectrum and the iron-line emission in the neutron-star LMXB 4U 1636−53 across different spectral states. We found that the temperature of the neutron star and that at the inner edge of the accretion disc increase, whereas the electron temperature of the corona decreases, as the source moves across the colour–colour diagram from the hard to the soft state. Simultaneously, the inner radius of the accretion disc deduced from the DISKBB component decreases rapidly by a factor of ∼10, and then remains more or less constant as the source reaches the soft state, suggesting that the inner edge of the disc may have reached the ISCO. The power-law photon index of the component used to fit the corona emission increases from ∼1.7 in the hard state up to ∼2.8 (depending on the model used to fit the line) in the soft state. Simultaneously, the total unabsorbed flux and the flux of the Comptonized component remain more or less constant, whereas the flux of the disc and that of the neutron star plus boundary layer increase, as the source moves from across the colour–colour diagram from the hard to the soft state (all fluxes calculated in the 0.5–130 keV range). Interestingly, the flux and equivalent width of the iron line first increase and then decrease as the flux of the Comptonized component increases. The maximum of this relation takes place when the source is close to the vertex in the colour–colour diagram.

The relation between the flux or the equivalent width of the line on one side and the flux of the hard spectral component on the other appears to contradict the expected behaviour if the line is due to reflection off the accretion disc. In the reflection scenario, the corona (and in neutron-star systems possibly also the neutron-star or boundary-layer) illuminates and photon-ions the disc, where the reflection spectrum (continuum + emission line) is then produced. In this scenario, the flux or equivalent width of the iron line should be positively correlated with that of the illuminating component. We find that, while this is the case when at low NTHCOMP flux values, the opposite is true when the NTHCOMP flux is high (see Fig. 10). However, the disc becomes more ionized when the illuminating flux increases, provided that there are enough photons with energies above the ionization potential of H- and He-like iron. As the flux of the illuminating component increases further, the material in the disc would eventually become fully ionized, and the line will disappear. This scenario agrees with recent calculations of the reflection spectrum of an ionized slab at different ionization levels (García et al. 2013). García et al. (2013) found (see their fig. 5) that the flux of the iron emission line in the reflected spectrum decreases gradually as the material in the slab is ionized further. Similarly, Matt, Fabian & Ross (1993) showed that the equivalent width of the iron line in the reflected spectrum of an ionized slab initially increases and then decreases as the flux of the ionizing source increases. Our results are generally consistent with this idea (compare our Fig. 10 with figs 1 and 2 in Matt et al. 1993). However, in this scenario, as the ionization state of the disc increases, the fitted energy of the emission line should gradually increase, as the fraction of H-like iron ions relative to the He-like iron ions in the disc increases. Our results do not show any correlation between the fitted energy of the line and the flux of the ionizing source (see Tables 4 and 5), regardless of the model we used to fit the line. While this lack of correlation could be due to limitations of the models that we used to fit the iron line, or to the fact that we only fitted the iron line instead of the full reflection spectrum, using the same *XMM–Newton* data presented here Sanna et al. (2013) found no correlation between the ionization parameter of the full reflection model they fitted to the spectra and the position of the source in the colour–colour diagram, reinforcing this conclusion.

Alternatively, the relation between iron-line flux or equivalent width and the flux of the hard spectral component in 4U 1636-53 shown in Fig. 10 could be interpreted in terms of light bending (Miniutti & Fabian 2004). In this model, the observed flux of the hard illuminating source (in our fits the NTHCOMP) depends strongly upon the height of the source of photons in the corona above the disc; the observed flux of the direct emission can change by up to a factor of ∼20 as the height of the illuminating source changes, even if the luminosity of the illuminating source remains constant. On the other hand, the reflected spectrum of the disc, and hence the flux or equivalent width of the iron line, is much less sensitive to the height of the illuminating source. Miniutti & Fabian (2004) find that there are three regimes in which, as the flux of the direct emission increases, the reflection component (and hence the iron-line flux or equivalent width) is first correlated, then insensitive, and finally anticorrelated with the flux of the direct emission. Rossi et al. (2005) found that, in the black hole candidate XTE J1650–500, as the total flux of the source above 7 keV increases, the flux of the iron line initially remains constant and eventually decreases. They found that the source flux level at which the line flux starts to decrease coincides with the transition from the hard to the soft state in this source. Park et al. (2004) also found a complex relation between the iron-line flux and the flux of the hard and the soft components in the black hole candidate 4U 1543–475. In this case, however, the relation does not follow any clear trend, and an interpretation in terms of the light bending model is not apparent. Rossi et al. (2005) suggested the direct and reflected components in XTE J1650–500 could be related to the existence of a radio jet in this source (Corbel et al. 2004), with possible changes of the height of the base of the jet as the mechanism that drives the changes of the direct emission in XTE J1650–500. It is unclear whether this could also be the case in 4U 1636-53, since this source has not been detected in radio, and hence the existence of a strong jet in this system is at best doubtful (Thomas et al. 1979; Russell et al. 2012). The lack of a strong radio jet in 4U 1636-53 could also be the reason that the flux of the hard (direct) component in this source changes only by a factor of ∼5, whereas in XTE J1650–500 the flux of the direct ionizing source changes by $\gtrsim$10. We finally note that if the relation between the flux or equivalent width of the iron line and the NTHCOMP flux in 4U 1636-53 is due to light

bending, this would be the first case of a neutron-star system in which this effect is observed. The light bending model was developed for the case of a rapidly spinning black hole, and therefore it is unclear whether it would also apply for a moderately spinning neutron star.

In the case of 4U 1636−53 the point at which the flux of the iron line switches from correlated to anticorrelated with the flux of the NTHCOMP component coincides with the vertex in the colour–colour diagram, at $S_a \sim 2.1$. The existence of the vertex in this diagram directly indicates a sudden change of the spectral properties of the source which, going from the hard to the soft state, quickly softens there. We note also that the vertex of the colour–colour diagram is the place where the quality factor of the kHz QPOs (Barret, Olive & Miller 2006; Méndez 2006) and the intrinsic coherence between the variability in the hard and soft energy bands (de Avellar et al. 2013) are the highest. Furthermore, Zhang et al. (2011) studied 298 type-I X-ray bursts in the 4U 1636−53 using *RXTE* observations, and they found that in this area of the colour–colour diagram most photospheric radius expansion bursts and a super-burst are observed. All these properties suggest that, in this source several properties of the accretion flow change significantly in this area of the colour–colour diagram.

The changes of the properties of the continuum spectrum of 4U 1636-53 as the source moves in the colour–colour diagram are generally consistent with those of other neutron-star LMXBs. For instance, Farinelli & Titarchuk (2011) measured the power-law index and the electron temperature kT_e of the Comptonizing component in the neutron-star LMXBs Sco X-1, GX 349+2, X 1658−298, 1E 1724−3045, GX 17+2, Cyg X−2, GX 340+0, GX 3+1, and GS 1826−238, and found that the power-law energy index ($\Gamma - 1$ in the NTHCOMP component) remains more or less constant at around 1±0.2. Using *RXTE* and *BeppoSAX* observations, Seifina & Titarchuk (2011, 2012) showed that in 4U 1728−34 and GX 3+1, the power-law index also remains almost constant as the temperature of the corona changes dramatically. Recently, Titarchuk, Seifina & Frontera (2013) found that in another neutron-star binary, 4U 1820−30, the power-law index remains almost constant for different source states. The power-law index in 4U 1636−53 changes from ∼1.7 in the hard state to ∼2.8 in the soft state (depending on the model used to fit the iron line), which is a somewhat larger than the variations in the sources studied by Farinelli & Titarchuk (2011, note, however, that the model that they used to fit the Comptonized component is not the same as the one we used here). Titarchuk et al. (2013) concluded that the power-law index quasi-stability is an intrinsic property of neutron-star binaries, which is fundamentally different from that of black hole binary systems. Seifina & Titarchuk (2011) suggested that this stability of the power-law index happens when the energy released in the corona itself is much higher than the one from the disc intercepted by the corona.

The changes of the continuum spectrum are also broadly consistent with the truncated disc scenario in LMXBs (e.g. Done et al. 2007, and references therein). The temperature of the disc increases and the inner radius of the disc decreases as the inferred mass accretion rate increases. The electron temperature of the NTHCOMP component and the temperature of the neutron-star surface are also consistent with this scenario. It is intriguing, however, that the inner radius of the accretion disc deduced from the relativistically broaden iron line does not follow the same trend. The model of the disc that we used to fit the data does not include spectral hardening, and the iron-line profile may be further affected by mechanisms other than relativistic broadening. It remains to be seen whether these effect could explain this discrepancy.

ACKNOWLEDGEMENTS

This research has made use of data obtained from the High Energy Astrophysics Science Archive Research Center (HEASARC), provided by NASA's Goddard Space Flight Center. This research made use of NASA's Astrophysics Data System. LM is supported by China Scholarship Council (CSC), grant number 201208440011. TMB acknowledges support from INAF PRIN 2012-6. We are grateful to Jon Miller for comments on a previous version of this manuscript.

REFERENCES

Altamirano D., van der Klis M., Méndez M., Jonker P. G., Klein-Wolt M., Lewin W. H. G., 2008, ApJ, 685, 436
Anders E., Grevesse N., 1989, Geochim. Cosmochim. Acta, 53, 197
Balucinska-Church M., McCammon D., 1992, ApJ, 400, 699
Barret D., Olive J. F., Oosterbroek T., 2003, A&A, 400, 643
Barret D., Olive J.-F., Miller M. C., 2006, MNRAS, 370, 1140
Basko M. M., 1978, ApJ, 223, 268
Belloni T., Homan J., Motta S., Ratti E., Méndez M., 2007, MNRAS, 379, 247
Bhattacharyya S., Strohmayer T. E., 2007, ApJ, 664, L103
Cackett E. M. et al., 2008, ApJ, 674, 415
Church M. J., Balucińska-Church M., 2001, A&A, 369, 915
Corbel S., Fender R. P., Tomsick J. A., Tzioumis A. K., Tingay S., 2004, ApJ, 617, 1272
de Avellar M. G. B., Méndez M., Sanna A., Horvath J. E., 2013, MNRAS, 433, 3453
Di Salvo T., Iaria R., Burderi L., Robba N. R., 2000a, ApJ, 542, 1034
Di Salvo T. et al., 2000b, ApJ, 544, L119
Done C., Gierliński M., Kubota A., 2007, A&AR, 15, 1
Dovčiak M., Karas V., Martocchia A., Matt G., Yaqoob T., 2004, in Hledík S., Stuchlík Z., eds, Proc. RAGtime 4/5, An XSPEC Model to Explore Spectral Features from Black-Hole Sources. Silesian University, Opava, p. 33
Fabian A. C., Ross R. R., 2010, Space Sci. Rev., 157, 167
Fabian A. C., Rees M. J., Stella L., White N. E., 1989, MNRAS, 238, 729
Farinelli R., Titarchuk L., 2011, A&A, 525, A102
Fiocchi M., Bazzano A., Ubertini P., Jean P., 2006, ApJ, 651, 416
Ford E. C., van der Klis M., Méndez M., Wijnands R., Homan J., Jonker P. G., van Paradijs J., 2000, ApJ, 537, 368
Frank J., King A., Raine D. J., 2002, Accretion Power in Astrophysics: 3rd edn. Cambridge Univ. Press, Cambridge
Galloway D. K., Psaltis D., Muno M. P., Chakrabarty D., 2006, ApJ, 639, 1033
García J., Dauser T., Reynolds C. S., Kallman T. R., McClintock J. E., Wilms J., Eikmann W., 2013, ApJ, 768, 146
Garson A. B., III, Baring M. G., Krawczynski H., 2010, ApJ, 722, 358
Gierliński M., Done C., 2003, MNRAS, 342, 1083
Gilfanov M., Revnivtsev M., Molkov S., 2003, A&A, 410, 217
Hasinger G., van der Klis M., 1989, A&A, 225, 79
Homan J. et al., 2007, ApJ, 656, 420
Iaria R., di Salvo T., Robba N. R., Lavagetto G., Burderi L., Stella L., van der Klis M., 2005, A&A, 439, 575
Kaaret P., Piraino S., Ford E. C., Santangelo A., 1999, ApJ, 514, L31
Laor A., 1991, ApJ, 376, 90
Lin D., Remillard R. A., Homan J., 2007, ApJ, 667, 1073
London R. A., Taam R. E., Howard W. M., 1986, ApJ, 306, 170
Madej J., Joss P. C., Różańska A., 2004, ApJ, 602, 904
Makishima K., Maejima Y., Mitsuda K., Bradt H. V., Remillard R. A., Tuohy I. R., Hoshi R., Nakagawa M., 1986, ApJ, 308, 635
Matt G., Fabian A. C., Ross R. R., 1993, MNRAS, 262, 179
McConnell M. L. et al., 2000, ApJ, 543, 928
Méndez M., 2006, MNRAS, 371, 1925
Méndez M., van der Klis M., 1999, ApJ, 517, L51

Méndez M., van der Klis M., van Paradijs J., Lewin W. H. G., Lamb F. K., Vaughan B. A., Kuulkers E., Psaltis D., 1997, ApJ, 485, L37
Méndez M., van der Klis M., Ford E. C., Wijnands R., van Paradijs J., 1999, ApJ, 511, L49
Miller J. M. et al., 2013, ApJ, 779, L2
Miniutti G., Fabian A. C., 2004, MNRAS, 349, 1435
Mitsuda K. et al., 1984, PASJ, 36, 741
Miyamoto S., Iga S., Kitamoto S., Kamado Y., 1993, ApJ, 403, L39
Oosterbroek T., Barret D., Guainazzi M., Ford E. C., 2001, A&A, 366, 138
Paizis A. et al., 2006, A&A, 459, 187
Pandel D., Kaaret P., Corbel S., 2008, ApJ, 688, 1288
Park S. Q. et al., 2004, ApJ, 610, 378
Pedersen H. et al., 1982, ApJ, 263, 325
Piraino S., Santangelo A., di Salvo T., Kaaret P., Horns D., Iaria R., Burderi L., 2007, A&A, 471, L17
Protassov R., van Dyk D. A., Connors A., Kashyap V. L., Siemiginowska A., 2002, ApJ, 571, 545
Rivers E. et al., 2010, ApJ, 709, 179
Rossi S., Homan J., Miller J. M., Belloni T., 2005, MNRAS, 360, 763
Russell D. M., O'Brien K., Muñoz-Darias T., Casella P., Gandhi P., Revnivtsev M. G., 2012, A&A, 539, A53
Sanna A., Hiemstra B., Méndez M., Altamirano D., Belloni T., Linares M., 2013, MNRAS, 432, 1144
Seifina E., Titarchuk L., 2011, ApJ, 738, 128
Seifina E., Titarchuk L., 2012, ApJ, 747, 99
Shakura N. I., Sunyaev R. A., 1973, A&A, 24, 337
Shih I. C., Bird A. J., Charles P. A., Cornelisse R., Tiramani D., 2005, MNRAS, 361, 602
Strohmayer T. E., Markwardt C. B., 2002, ApJ, 577, 337
Sunyaev R. A., Titarchuk L. G., 1980, A&A, 86, 121
Thomas R. M. et al., 1979, MNRAS, 187, 299
Titarchuk L., Seifina E., Frontera F., 2013, ApJ, 767, 160
Ushio M. et al., 2009, ApJ, 699, 1964
van Straaten S., van der Klis M., Méndez M., 2003, ApJ, 596, 1155
White N. E., Stella L., Parmar A. N., 1988, ApJ, 324, 363
Wijnands R. A. D., van der Klis M., van Paradijs J., Lewin W. H. G., Lamb F. K., Vaughan B., Kuulkers E., 1997, ApJ, 479, L141
Yoshida K., Mitsuda K., Ebisawa K., Ueda Y., Fujimoto R., Yaqoob T., Done C., 1993, PASJ, 45, 605
Zdziarski A. A., Johnson W. N., Magdziarz P., 1996, MNRAS, 283, 193
Zhang W., Lapidus I., White N. E., Titarchuk L., 1996, ApJ, 469, L17
Zhang W., Lapidus I., Swank J. H., White N. E., Titarchuk L., 1997, IAU Circ., 6541, 1
Zhang G., Méndez M., Altamirano D., Belloni T. M., Homan J., 2009, MNRAS, 398, 368
Zhang G., Méndez M., Altamirano D., 2011, MNRAS, 413, 1913
Życki P. T., Done C., Smith D. A., 1999, MNRAS, 309, 561

This paper has been typeset from a TEX/LATEX file prepared by the author.